Elimination of remnant phases in low-temperature growth of wurtzite ScAlN by molecularbeam epitaxy

Brandon Dzuba^{1,2}, Trang Nguyen¹, Amrita Sen³, Rosa E. Diaz², Megha Dubey⁴, Mukesh Bachhav⁵, Janelle P. Wharry³, Michael J. Manfra^{1,2,3,6}, Oana Malis^{1,2*}

¹Department of Physics and Astronomy, Purdue University, West Lafayette, Indiana 47907, USA

²Birck Nanotechnology Center, West Lafayette, Indiana 47907, USA

³School of Materials Engineering, Purdue University, West Lafayette, Indiana 47907, USA

⁴Center for Advanced Energy Studies, Idaho Falls, ID 83401

⁵Idaho National Laboratory, Materials and Fuel Complex, Scoville, ID 83415

⁶School of Electrical and Computer Engineering, Purdue University, West Lafayette, Indiana 47907, USA

Growth of wurtzite Sc_xAl_{1-x}N (x < 0.23) by plasma-assisted molecular-beam epitaxy on c-plane GaN at high temperatures significantly alters the extracted lattice constants of the material due to defects likely associated with remnant phases. In contrast, ScAlN grown below a composition-dependent threshold temperature exhibits uniform alloy distribution, reduced defect density, and atomic-step surface morphology. The c-plane lattice constant of this low-temperature ScAlN varies with composition as expected from previous theoretical calculations, and can be used to reliably estimate alloy composition. Moreover, lattice-matched Sc_{0.18}Al_{0.82}N/GaN multi-quantum wells grown under these conditions display strong and narrow near-infrared intersubband absorption lines that confirm advantageous optical and electronic properties.

1

^{*} Author to whom correspondence should be addressed. Electronic mail: omalis@purdue.edu

1. Introduction

Aluminum nitride (AIN), indium nitride (InN), and gallium nitride (GaN) have been major topics of interest in the materials and device communities in recent decades primarily due to the large range of bandgaps achievable using III-nitride alloys (0.64 eV - 6.2 eV). These materials have been used in the development of various electronic and optoelectronic devices such as light-emitting diodes, laser diodes, and high electron mobility transistors (HEMTs)¹. A persistent challenge throughout these III-nitride devices, however, is the large lattice mismatch between different alloys that can exceed 9% in InN/GaN heterostructures. The resulting strain leads to formation of defects that are detrimental to device performance. A potential solution to this problem is to utilize materials that are lattice-matched to the substrate, such as In_{0.17}Al_{0.83}N layers on GaN. Unfortunately, In_{0.17}Al_{0.83}N layers have been plagued with severe inhomogeneity issues²⁻⁶ that negatively impact optical characteristics.⁷⁻¹⁰ Here, we investigate the structure and optical properties of the novel material wurtzite ScAIN, focusing on the Sc composition range around 18 at. % that is lattice-matched to c-plane GaN.

ScAlN has recently attracted attention due to its wide applicability in a variety of devices. ScAlN's large bandgap, spontaneous polarization,⁷ and dielectric permittivity⁸ can yield high two-dimensional electron gas densities, making it an attractive material for HEMTs and heterostructure field effect transistors (HFETs).^{9–12} The enhanced electromechanical coupling of ScAlN relative to AlN¹³ make the material ideal for electroacoustic resonators.^{14–18} Furthermore, the significantly reduced etch rate of ScAlN compared to GaN and AlN make it suitable as an etch-stop layer for device fabrication.¹⁹ Lastly, ScAlN is also emerging as a candidate for memory storage devices. ScAlN's slow shift of its internal lattice parameter with increasing scandium composition has been shown to facilitate polarization switching²⁰ with polarization retention times exceeding 10⁵ seconds.²¹

Many of the unique properties of ScAIN originate from its distinctive structural instability.²²⁻
²⁸ Unlike the commonly-studied III-nitrides, Sc_xAI_{1-x}N is stable in the wurtzite crystal phase only

below $x \approx 0.55$, and transitions to a rock-salt phase at higher Sc composition. ^{20,22,23} A metastable nonpolar hexagonal, or h-BN-like phase, has also been proposed theoretically for ScN and ScAIN, but has not been confirmed experimentally²⁴. Key material parameters of wurtzite ScAIN were first measured on polycrystalline sputter-deposited films, 7,25-27 and calculated using density functional theory. 25-27 Structural parameters (lattice constants, stiffness coefficients, internal cell parameter, and bond angles) and other material parameters (dielectric constant, spontaneous polarization, and piezoelectric coefficients) are all believed to vary non-linearly with composition, ^{26,28} but the scattering of reported experimental values may be due to differences in composition determination or mixed phases in the sputter-deposited material. Most notably, the change in bond angles and average bond lengths of relaxed wurtzite ScAIN with increasing Sc composition results in a relatively small and non-monotonic change in c-plane lattice constant.²⁷ This makes the determination of alloy composition using the typical method of x-ray diffraction (XRD) problematic. Estimation of the scandium mole-fraction in ScAIN layers by XRD is further complicated by the reported growth-temperature dependence of the c-plane lattice constant.^{29,30} Hardy et al. observed a monotonic increase of the XRD symmetric scan ω-2Θ peak angle with growth-temperature in $Sc_xAl_{1-x}N$ ($x \approx 0.18$) layers grown on N-polar GaN substrates by molecularbeam epitaxy (MBE), despite little to no change in material composition. Under the circumstances, accurate estimation of the composition of ScAIN has been limited to time-consuming and expensive techniques such as Rutherford backscattering (RBS), energy dispersive x-ray spectroscopy (EDS), and x-ray photoelectron spectroscopy (XPS).

In this work we seek to understand the link between growth temperature and crystalline structure in ScAIN, as well as to provide a framework for reliable compositional estimation of ScAIN by standard XRD techniques. We investigate wurtzite $Sc_xAI_{1-x}N$ growth by MBE on Ga-face (0001)-oriented GaN substrates across a range of compositions ($x \approx 0.11 - 0.23$) and growth temperatures (450°C - 760°C). At high growth temperatures, for all compositions tested, we observe a dependence of the c-plane lattice constants in ScAIN on growth temperature, similar

to that reported by Hardy et al. for Sc_{0.18}Al_{0.82}N.²⁹ Additionally, we find that the lattice constants of ScAlN grown at low temperature can be well explained by theory,²⁶ while those of high temperature ScAlN deviate significantly from theoretical predictions. Higher growth temperatures result in 3D growth, higher defect densities, higher surface roughness, and an inhomogeneous distribution of atoms within the material. These results may explain the deviation from theoretical lattice constants at higher temperatures. Lastly, we report for the first time near-infrared intersubband absorption with extremely narrow lines in lattice-matched Sc_{0.18}Al_{0.82}N/GaN multiple quantum wells (MQW). This demonstrates the outstanding material and optical properties of low growth temperature MBE grown ScAlN, making it a promising material for future device applications.

2. Experimental

All nitride structures were grown by plasma-assisted MBE (PAMBE) on commercially available semi-insulating c-plane (0001)-oriented GaN on sapphire substrates with a reported treading dislocation density of 8×10⁸ cm⁻². The substrates were backside coated in 1 μm of tungsten silicide for improved thermal coupling and diced into quarters. Prior to loading into an ultra-high vacuum (UHV) environment, the substrates were etched for 10 minutes in boiling HCl to remove any excess metals, sonicated in trichloroethylene, acetone, and methanol to remove any organic materials, and then rinsed with deionized water and dried with N₂ gas. The substrates were outgassed overnight (> 12 hours) at 550°C in an UHV chamber attached to the MBE. The PAMBE system is equipped with conventional effusion cells for aluminum, indium, gallium, scandium, and silicon. A scandium source of 99.999% purity was used to reduce the reported negative effects of carbon, oxygen, and fluorine impurities.^{31,32} A Veeco Unibulb radio-frequency (RF) plasma source is used to supply active nitrogen to the substrate. Prior to the active layer, a 150 nm GaN buffer layer is grown at 720°C under gallium-rich conditions. This results in a GaN

surface with pronounced atomically-flat terraces and root-mean square (RMS) roughness < 0.3 nm over 4 μ m², as measured by atomic force microscopy (AFM) on control samples.

A series of 30-40 nm Sc_xAl_{1-x}N films was grown across a range of compositions (0.11 < x < 0.23) and growth temperatures (450°C – 760°C) as measured by pyrometer. All Sc-containing layers were grown within the nitrogen-rich regime, as metal-rich growth results in poor surface and structural quality³³ and the development of intermetallic phases on the surface.³⁴ The individual ScAlN films were grown with a III/V ratio between 0.6 and 0.8, while the ScAlN used in the MQW structures used a III/V ratio of approximately 0.9. Plasma conditions of 305 W RF power with a 0.5 sccm N₂ flow rate were used to generate an active nitrogen flux of ≈ 5.8x10¹⁴ atoms/cm²s, giving a nitrogen-limited GaN growth rate of approximately 7.9 nm/min. The MQW structures consisted of 50 repeats of Sc_{0.18}Al_{0.82}N/GaN followed by an additional ScAlN barrier to form the last quantum well (QW), and employed the gallium-rich growth method for the GaN layers. Excess gallium was incorporated into the structure by exposure to active nitrogen after each GaN layer. All MQWs were doped with silicon using a δ-doping scheme in which two sheets of silicon are placed inside the ScAlN barrier approximately one nanometer from each interface.

X-ray diffraction (XRD) reciprocal space mapping (RSM) and rocking curve measurements were made with a Panalytical Empyrean High-Resolution diffractometer, while XRD symmetric ω -2 Θ scans were taken using a Panalytical X'Pert³ MRD. Material thicknesses and MQW periods were determined either from thickness fringes in XRD symmetric ω -2 Θ scans or by high-angle annular dark-field scanning transmission electron microscopy (HAADF-STEM) imaging. ScAIN material composition was determined by Rutherford backscattering (RBS) measurements conducted by EAG Laboratories, with an uncertainty in the scandium composition of ±1 at.%. The surface morphology of all samples was assessed using AFM.

MQW c-plane structures were investigated with HAADF-STEM. Acquisition was done with a double aberration-corrected Thermo Scientific Themis Z TEM/STEM at 300kV acceleration voltage, 0.24 nA current, and 0.65 Å probe size. STEM samples were prepared using the focused

ion beam (FIB) *in situ* lift-out method on a Thermo Scientific Helios G4 UX Dual Beam FIB. Following the FIB process, the specimens were further thinned using a Fischione Nanomill Model 1040, working at 900 V, 120 μ A, and $\pm 10^{\circ}$ tilt at low temperature. Finally, each lamella was cleaned with a Fischione Ar Plasma Cleaner to remove any residue from the FIB and air.

Atom probe tomography (APT) was conducted to determine the chemical homogeneity of two Sc_{0.18}Al_{0.82}N samples grown at different temperatures (550°C and 720°C). Specimens for APT were prepared by FIB milling. Due to the tendency of preferential evaporation of Ga during APT,^{35–37} liftouts were made in cross-section from the sample. All FIB work was done on the FEI (now Thermo Fisher Scientific) Quanta 3D FEG dual-beam FIB at the Center for Advanced Energy Studies (CAES), Idaho National Laboratory. Samples were analyzed using the CAMECA Local Electrode Atom Probe (LEAP) 4000X HR equipped with 355 nm UV laser, also at CAES. Specimens were analyzed under a wide range of LEAP running conditions selected to systematically investigate the influence of key parameters on the evaporation behavior and composition measurements, but ultimately the conditions of 0.1 pJ laser energy, 45 K base temperature, 200 kHz pulse rate, and 0.5% detection rate were chosen to minimize Ga preferential evaporation effects. A minimum of 2 million ions were collected per needle to ensure statistical significance. APT data was processed and analyzed through CAMECA's Integrated Visualization and Analysis Software (IVAS version 3.8.4). Peaks in the APT mass spectra were ranged according to traditional mass ranging methods.³⁸

Using a Thermo Scientific Nicolet 8700 spectrometer, direct Fourier transform infrared spectroscopy (FTIR) was utilized to measure intersubband absorption (ISBA) on all MQW samples. The samples were polished into small pieces with 45° facets on both sides to let electromagnetic waves enter and be absorbed by the active region. The ISBA spectra were obtained by first normalizing the p- and s-polarized transmission spectra to the background, followed by calculating the ratio of the p- to s-polarized transmission spectra.

3. Results and Discussion

Figure 1 summarizes the dependence of ScAIN lattice constants for the out-of-plane (0001) direction (c-axis) and in-plane ($11\overline{2}0$) direction (a-axis) on Sc composition and growth temperature (see Supplementary information for XRD RSM). Theoretical predictions for the wurtzite lattice constants are also included as curves in Fig. 1 both for ScAIN fully strained to GaN (red lines) and fully relaxed ScAIN (blue lines). These curves were obtained using the known values of the AIN lattice constants and the stiffness coefficients reported in Ambacher et al.²⁶ and Urban et al.²⁷ In agreement with previous reports, 29,30 we find $Sc_xAI_{1-x}N$ (x ≈ 0.18) grown at 720°C to have an average c-plane lattice constant smaller than films grown at or below 550°C. The effect is also clearly visible as a shift of the ScAIN XRD ω -2 Θ peak towards larger angles (Fig. S4). This unusual behavior cannot be explained by theory that predicts wurtzite Sc_{0.18}Al_{0.82}N to be in-plane lattice-matched to GaN, and therefore no elastic strain is expected at this composition. Residual strain due to thermal expansion mismatch also cannot justify the magnitude of this effect. Furthermore, we find the same correlation between c-plane lattice constant and growth temperature across a broad range of compositions (0.11 < x < 0.23) and growth temperatures (450°C – 760°C). Specifically, for all but the lowest investigated composition, growth temperatures above 700°C result in c-plane lattice constants significantly lower than theoretically predicted for either strained or relaxed ScAIN. For the largest Sc composition investigated (x \approx 0.22), this cplane lattice constant is even smaller than the value for pure AIN tensile-strained to GaN. We attribute the lower c-plane lattice constant to the existence of structural defects that are remnant of the non-polar hexagonal h-ScN phase. The signature of this h-BN-like phase is a c/a ratio smaller than the value for the wurtzite structure (1.63); a reduction of the c/a ratio has been previously observed in sputter-deposited ScAIN films.²⁰

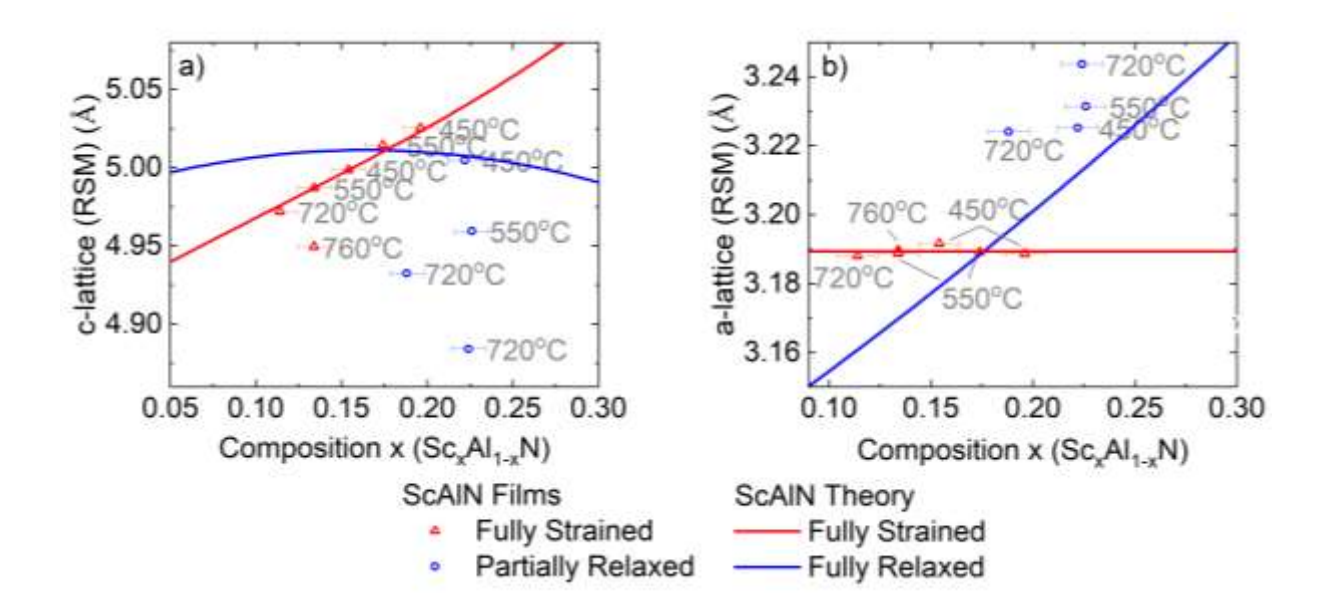


Figure 1. (0001) c-plane lattice constants (a), and ($11\overline{2}0$) a-plane lattice constants (b) of ScAlN films determined from XRD RSM. The 30-40 nm thick ScAlN films have compositions near x ≈ 0.12, 0.18, 0.22, and were grown at temperatures of 450°C, 550°C, 720°C or 760°C, as indicated on the figure. The films were either fully coherent to the underlying GaN (red triangles) or exhibited some degree of relaxation (blue circles). Red and blue lines represent the theoretical lattice constants for ScAlN grown on GaN substrates, assuming either fully coherent or fully relaxed films, respectively. Error bars represent error in film composition determined by RBS measurements.

Fig. 1 also indicates the strain state of the films extracted from RSM; coherently strained films use red symbols while partially relaxed films use blue symbols. For Sc composition above 20%, all films are partially relaxed regardless of growth temperature. At the highest growth temperatures, the measured c-plane lattice constant is significantly smaller than the expected value when the measured tensile strain state is considered. Moreover, the in-plane lattice constants of partially relaxed films are larger than expected for fully relaxed ScAIN (Fig. 1(b)).

This suggests that the deformation indicated by Figure 1 is not solely due to changes in the strain state of the films, but must be caused by additional structural defects.

The available data suggests that below a composition-dependent growth temperature, the measured c-plane lattice constants for coherently strained ScAIN agree well with the values predicted by theory (red line). This is true for films with scandium compositions $x \approx 0.12$ and $x \approx 0.18$ grown at and below 720°C and 550°C, respectively. Therefore, the composition of Sc_xAI_{1-x}N films grown at low temperature can be reliably predicted for $x \leq 0.2$ from XRD ω -2 Θ scans. We note that film coherence to the substrate is a necessary, but not sufficient condition for the use of this composition determination method. For x > 0.2, the ScAIN films are partially relaxed, regardless of growth temperature, and composition needs to be determined using either RBS, EDS, or XPS.

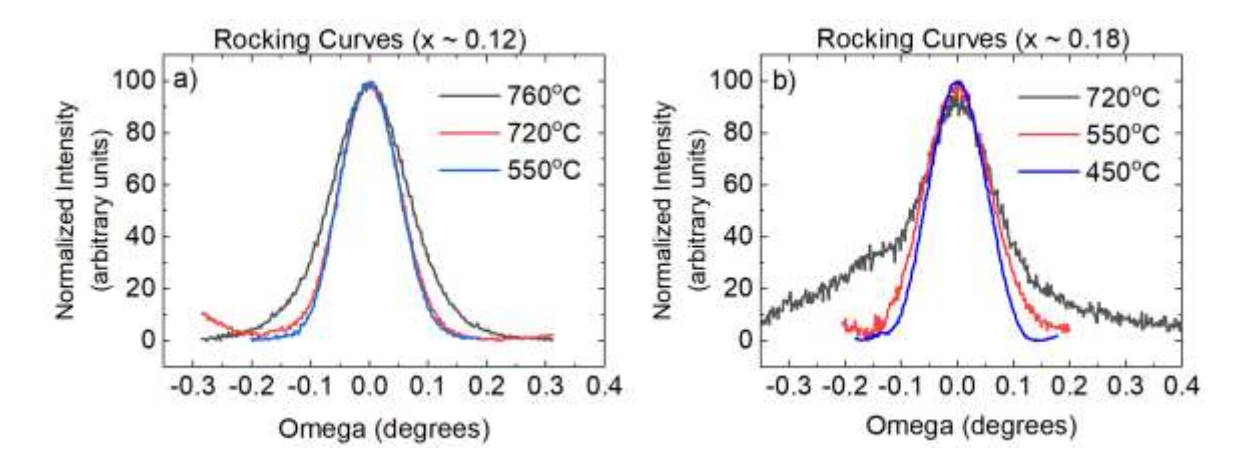


Figure 2. XRD rocking curves of (0002) reflections for the ScAIN layers. (a) ScAIN layers with $x \approx 0.12$, grown at 760°C, 720°C, and 550°C, exhibit FWHM of 0.155°, 0.118°, and 0.116°. (b) ScAIN layers with $x \approx 0.18$ grown at 720°C, 550°C, and 450°C exhibit FWHM of 0.167°, 0.136°, and 0.118°. Note that rocking curves were not measured for samples with x > 0.2 as the reduced intensity of the ScAIN XRD peak, coupled with the proximity to the intense GaN peak, made measurement of the peak impossible.

To further examine the effect of growth temperature on defect densities, XRD rocking curves were measured for the x \approx 0.12 and x \approx 0.18 films (Figure 2). We were unable to measure rocking curves for films with x > 0.2 due to the low intensity of the ScAIN peak coupled with its proximity to the intense GaN peak. For both compositions, the FWHM decreases with decreasing growth temperature. This trend confirms that growth at higher temperatures introduces defects into the material. The lowest growth-temperature samples have FWHM < 430 arcseconds, similar to that reported by Wang et al. ³⁰ AFM was also conducted on each film to assess surface morphology. AFM of all structures (see supplementary material) grown at 550°C presents atomic steps, indicating a step-flow growth mode. These films have an RMS surface roughness < 0.9 nm over a 4 μ m². Surface steps are not visible for any composition at growth temperatures above 550°C, and further reduction below 550°C results in less-defined atomic steps. The absence of atomic steps at higher growth temperatures reinforces the conclusion drawn from XRD data; lower growth temperatures result in higher-quality ScAIN.

Since compositional fluctuations can cause phase segregation, we utilized APT to assess the chemical variations within the ScAIN films. Two 100 nm Sc_{0.18}Al_{0.82}N films capped with 250 nm GaN were grown at 550°C and 720°C for APT measurements. The frequency distribution analyses from APT tip reconstructions are presented in Figure 3. The film grown at 550°C has a uniform distibution of all atomic species, shown by the excellent fit between the experimental data and a binomial distibution (Figure 3(a,b)). The 720°C film, however, shows an inhomogeneous distribution of aluminum atoms, with regions of lower AI atom number density (Figure 3(c,d)). In contrast, the Sc atom number density variation is smaller than that of AI atoms. Due to the non-monotonic dependence of c-plane lattice constants on Sc composition, higher Sc composition regions relative to the matrix could result in a lower average lattice constant, as seen in Figure 1. High concentration ScAIN could also result in the formation of rock-salt regions,²⁰ but we found no evidence of this phase in high-resolution STEM.

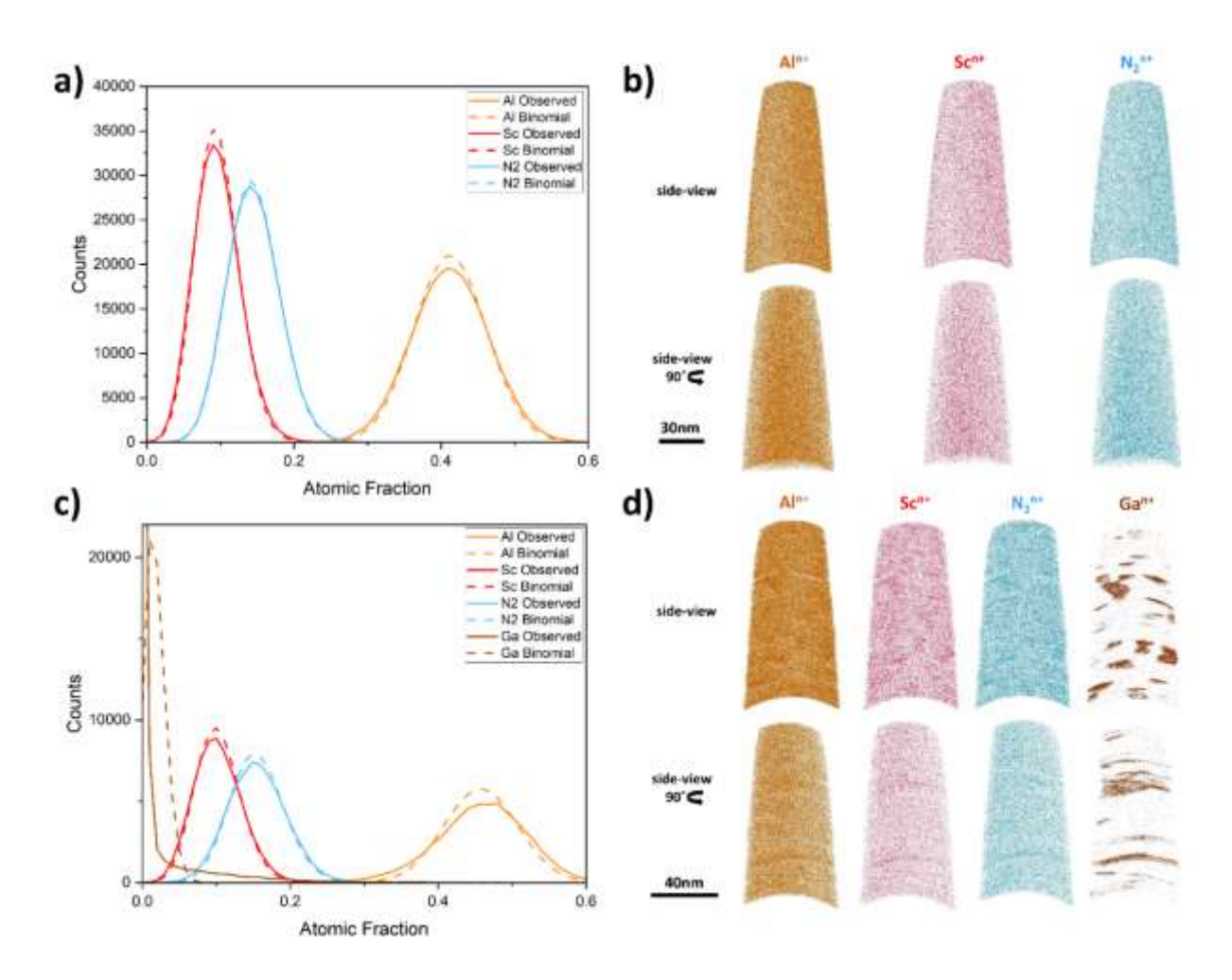


Figure 3. APT frequency distribution of the ionic species and cross-sectional atomic density maps in Sc_{0.18}Al_{0.82}N films grown at 550°C (a and b) and 720°C (c and d). Deviation from binomial distribution indicates a non-uniform distribution of elements.

Surprisingly, gallium atoms were also detected in the Sc_{0.18}Al_{0.82}N layer grown at 720°C. APT compositional analysis shows that these Ga-containing regions may reach a composition as high as 20 at. % Ga (see supplementary material). These nanometer-size regions were observed in all the 720°C tips analyzed and are not a product of any gallium contamination from FIB preparation, as the gallium source used for FIB preparation is monoisotopic and would show a single peak (69 Da) in the mass spectra.³⁹. While a detailed analysis of these Ga-rich regions is outside the scope of this work, we suspect they are linked to defect generation at high growth

temperatures that facilitates Ga diffusion into ScAlN during GaN cap deposition. The inclusion of even a small fraction of gallium could form ScGaN alloys, that separate into zinc-blende phases even at low scandium compositions. These Ga-containing defective phases likely alter the average lattice constant of the material as we have seen in this report. Since the presence of these remnant defects is deleterious for the optical and electronic properties ScAlN, it is preferable to supress them altogether by focusing on low-temperature MBE growth. It is important to emphasize that these Ga-containing phases were not present in the films grown at 550°C.

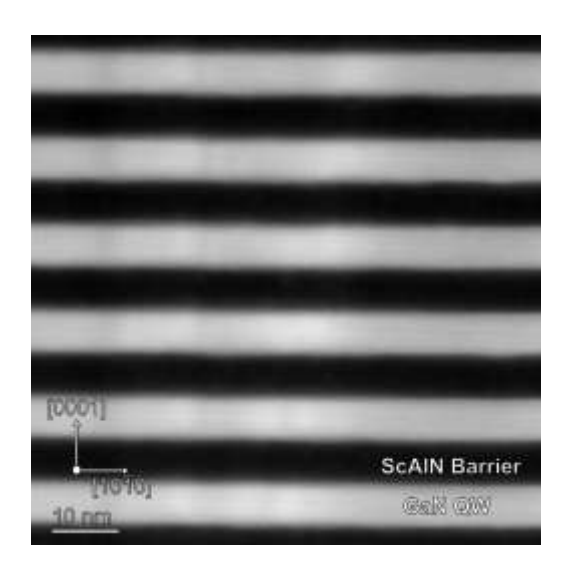


Figure 4. Dark-field HR-STEM of a $Sc_{0.18}AI_{0.82}N/GaN$ (7 nm \times 6 nm) MQW heterostructure with a silicon sheet density of 1.15×10^{13} cm⁻². Dark regions represent the ScAIN barriers, while light regions represent the GaN QWs.

Figure 5. Direct Fourier transform infrared (FTIR) absorption measurements of 50 repeat $Sc_{0.18}Al_{0.82}N/GaN$ MQWs (QW width 4, 6, and 8 nm) with barrier width of 7 nm and a silicon sheet density of 1.15×10^{13} cm⁻².

To asses the potential of low-temperature ScAlN for optical devices, we investigated near-infrared intersubband absorption in lattice-matched $Sc_{0.18}Al_{0.82}N/GaN$ MQW heterostructures. HR-STEM of one of the $Sc_{0.18}Al_{0.72}N/GaN$ heterostructures is shown in Figure 4. HR-STEM reveals abrupt interfaces and a regular periodic structure. A series of MQWs was grown with a constant doping profile (silicon sheet density of 1.15×10^{13} cm⁻²) but varying QW width (Figure 5). QW widths of 8 nm, 6 nm, and 4 nm resulted in ISBA energies of 523 meV, 567 meV, 611 meV with FWHM of 52 meV, 50 meV, and 45 meV, respectively. This trend of reduced ISBA energy with increasing QW width confirms that the absorption is due to intersubband transitions, while the narrow FWHM confirms the excellent structural quality. To the authors' knowledge, this is the first demonstration of near-IR ISBA in ScAlN/GaN MQW structures.

4. Conclusion

Wurtzite Sc_xAl_{1-x}N (x < 0.23) with outstanding structural and optical properties was grown by standard PAMBE at temperatures lower than typically used for Al(Ga)N. We investigated a series of 30-40 nm thick ScAlN films grown on Ga-face (0001)-oriented GaN/sapphire substrates across a range of scandium compositions (0.11 < x < 0.23) and growth temperatures (450°C – 760°C). The lattice parameters of these films were extracted from XRD RSM and compared to theoretical predictions. For all except the lowest composition studied (x = 0.11), we find a correlation between the c-plane lattice constant and growth temperature. The c-plane lattice constant of films grown at high temperature (i.e. typically above 700°C) is smaller than the value predicted by theory, and smaller than the lattice constant of films grown at low temperatures. RSM measurements verify that this variation of c-plane lattice constant is not due to elastic relaxation in the material. XRD rocking curves indicate that higher growth temperatures lead to the generation of additional defects. In contrast, for low growth temperatures, the c-plane lattice constants agree with theoretical predictions, suggesting that XRD techniques can be used to reliably estimate the composition of coherently strained films with x < 0.2. This also eliminates the need to perform

more sophisticated composition analysis. Moreover, the surface morphology also improves at lower growth temperatures, with pronounced atomic steps visible for all films grown at 550°C. APT analysis of two Sc_{0.18}Al_{0.82}N films grown at different temperatures shows a drastic increase in material homogeneity at 550°C, and severe chemical inhomogeneity present in the sample grown at 720°C. We conclude that high temperature growth leads to defect generation in MBE grown ScAlN, that may cause the observed temperature dependence of the c-plane lattice parameter.

Using the optimal growth conditions for Sc_{0.18}Al_{0.82}N, a series of silicon-doped lattice-matched ScAlN/GaN MQWs was grown and near-infrared ISBA was measured to probe the existence of well-defined confined electronic states. Strong and narrow near-infrared absorption lines are observed for the first time in Sc-containing nitride heterostructures. These optical results demonstrate the high quality of low-temperature ScAlN and reinforce its relevance for a wide range of devices.

Supplementary Material

See the supplementary material for RSM scans and AFM images of the 30-40 nm ScAIN films. Supplementary material also includes XRD symmetric ω -2 Θ scans for the x \approx 0.18 ScAIN films and APT composition profiling of the 720°C, x \approx 0.18, 100 nm thick film.

Acknowledgements

We acknowledge support from the National Science Foundation (NSF). T.N. and O.M. acknowledge partial support from NSF award DMR-2004462. A.S., M.B., and J.P.W. acknowledge partial support from the Center for Thermal Energy Transport Under Irradiation, an Energy Frontier Research Center funded by the U.S. Department of Energy, Office of Science, Basic Energy Sciences. All STEM imaging and analyses were performed at the Electron Microscopy Facility at the Birck Nanotechnology Center, Purdue University. APT characterization

was performed at the Center for Advanced Energy Studies, with support from the U.S. Department of Energy, Office of Nuclear Energy, through Nuclear Science User Facilities (NSUF) award 20-2946.

Data Availability

The data that supports the findings of this study are available within the article.

References

- ¹ O. Ambacher, J. Phys. D: Appl. Phys. **31**, 2653 (1998).
- ² S. Choi, F. Wu, R. Shivaraman, E.C. Young, and J.S. Speck, Appl. Phys. Lett. **100**, 232102 (2012).
- ³ S. Dasgupta, S. Choi, F. Wu, J.S. Speck, and U.K. Mishra, Appl. Phys. Express **4**, 045502 (2011).
- ⁴ W. Kong, W.Y. Jiao, J.C. Li, K. Collar, J.H. Leach, J. Fournelle, T.H. Kim, and A.S. Brown, J. Elec. Mater. **45**, 654 (2016).
- ⁵ L. Zhou, D.J. Smith, M.R. McCartney, D.S. Katzer, and D.F. Storm, Appl. Phys. Lett. **90**, 081917 (2007).
- ⁶ S.-L. Sahonta, G.P. Dimitrakopulos, Th. Kehagias, J. Kioseoglou, A. Adikimenakis, E. Iliopoulos, A. Georgakilas, H. Kirmse, W. Neumann, and Ph. Komninou, Appl. Phys. Lett. **95**, 021913 (2009).
- ⁷ M.A. Caro, S. Zhang, T. Riekkinen, M. Ylilammi, M.A. Moram, O. Lopez-Acevedo, J. Molarius, and T. Laurila, J. Phys.: Condens. Matt. **27**, 245901 (2015).
- ⁸ J. Casamento, H. Lee, T. Maeda, V. Gund, K. Nomoto, L. van Deurzen, W. Turner, P. Fay, S. Mu, C.G. Van de Walle, A. Lal, H. (Grace) Xing, and D. Jena, Appl. Phys. Lett. **120**, 152901 (2022).

- ⁹ A.J. Green, J.K. Gillespie, R.C. Fitch, D.E. Walker, M. Lindquist, A. Crespo, D. Brooks, E. Beam, A. Xie, V. Kumar, J. Jimenez, C. Lee, Y. Cao, K.D. Chabak, and G.H. Jessen, IEEE Elec. Dev. Lett. **40**, 1056 (2019).
- ¹⁰ P. Wang, D. Wang, B. Wang, S. Mohanty, S. Diez, Y. Wu, Y. Sun, E. Ahmadi, and Z. Mi, Appl. Phys. Lett. **119**, 082101 (2021).
- ¹¹ A.J. Green, N. Moser, N.C. Miller, K.J. Liddy, M. Lindquist, M. Elliot, J.K. Gillespie, R.C. Fitch, R. Gilbert, D.E. Walker, E. Werner, A. Crespo, E. Beam, A. Xie, C. Lee, Y. Cao, and K.D. Chabak, IEEE Elec. Dev. Lett. 41, 1181 (2020).
- ¹² T.E. Kazior, E.M. Chumbes, B. Schultz, J. Logan, D.J. Meyer, and M.T. Hardy, in *2019 IEEE MTT-S International Microwave Symposium (IMS)* (2019), pp. 1136–1139.
- ¹³ G. Wingqvist, F. Tasnádi, A. Zukauskaite, J. Birch, H. Arwin, and L. Hultman, Appl. Phys. Lett. **97**, 112902 (2010).
- ¹⁴ W. Wang, P.M. Mayrhofer, X. He, M. Gillinger, Z. Ye, X. Wang, A. Bittner, U. Schmid, and J.K. Luo, Appl. Phys. Lett. **105**, 133502 (2014).
- ¹⁵ W.B. Wang, Y.Q. Fu, J.J. Chen, W.P. Xuan, J.K. Chen, X.Z. Wang, P. Mayrhofer, P.F. Duan, A. Bittner, U. Schmid, and J.K. Luo, J. Micromech. Microeng. **26**, 075006 (2016).
- ¹⁶ R. Dargis, A. Clark, A. Ansari, Z. Hao, M. Park, D. Kim, R. Yanka, R. Hammond, M. Debnath, and R. Pelzel, Phys. Stat. Sol. (a) **217**, 1900813 (2020).
- ¹⁷ A. Ding, L. Kirste, Y. Lu, R. Driad, N. Kurz, V. Lebedev, T. Christoph, N.M. Feil, R. Lozar, T. Metzger, O. Ambacher, and A. Žukauskaitė, Appl. Phys. Lett. **116**, 101903 (2020).
- ¹⁸ V.J. Gokhale, B.P. Downey, M.T. Hardy, E.N. Jin, J.A. Roussos, and D.J. Meyer, in *2020 IEEE 33rd International Conference on Micro Electro Mechanical Systems (MEMS)* (IEEE, Vancouver, BC, Canada, 2020), pp. 1262–1265.
- ¹⁹ M.T. Hardy, B.P. Downey, D.J. Meyer, N. Nepal, D.F. Storm, and D.S. Katzer, IEEE Transactions on Semiconductor Manufacturing **30**, 475 (2017).

- ²⁰ S. Zhang, D. Holec, W.Y. Fu, C.J. Humphreys, and M.A. Moram, J. Appl. Phys. **114**, 133510 (2013).
- ²¹ P. Wang, D. Wang, N.M. Vu, T. Chiang, J.T. Heron, and Z. Mi, Appl. Phys. Lett. **118**, 223504 (2021).
- ²² S. Barth, H. Bartzsch, D. Gloess, P. Frach, T. Modes, O. Zywitzki, G. Suchaneck, and G. Gerlach, in edited by J.L. Sánchez-Rojas and R. Brama (Barcelona, Spain, 2015), p. 951704.
- ²³ R. Deng, S.R. Evans, and D. Gall, Appl. Phys. Lett. **102**, 112103 (2013).
- ²⁴ N. Farrer and L. Bellaiche, Phys. Rev. B **66**, 201203 (2002).
- ²⁵ S. Zhang, W.Y. Fu, D. Holec, C.J. Humphreys, and M.A. Moram, J. Appl. Phys. **114**, 243516 (2013).
- ²⁶ O. Ambacher, B. Christian, N. Feil, D.F. Urban, C. Elsässer, M. Prescher, and L. Kirste, J. Appl. Phys. **130**, 045102 (2021).
- ²⁷ D.F. Urban, O. Ambacher, and C. Elsässer, Phys. Rev. B **103**, 115204 (2021).
- ²⁸ F. Tasnádi, B. Alling, C. Höglund, G. Wingqvist, J. Birch, L. Hultman, and I.A. Abrikosov, Phys. Rev. Lett. **104**, 137601 (2010).
- ²⁹ M.T. Hardy, B.P. Downey, N. Nepal, D.F. Storm, D.S. Katzer, and D.J. Meyer, Appl. Phys. Lett. **110**, 162104 (2017).
- ³⁰ P. Wang, D.A. Laleyan, A. Pandey, Y. Sun, and Z. Mi, Appl. Phys. Lett. **116**, 151903 (2020).
- ³¹ J. Casamento, H. Lee, C.S. Chang, M.F. Besser, T. Maeda, D.A. Muller, H. (Grace) Xing, and D. Jena, APL Materials **9**, 091106 (2021).
- ³² J. Casamento, H.G. Xing, and D. Jena, Phys. Status Solidi B-Basic Solid State Phys. **257**, 1900612 (2020).
- ³³ M.T. Hardy, E.N. Jin, N. Nepal, D.S. Katzer, B.P. Downey, V.J. Gokhale, D.F. Storm, and D.J. Meyer, Appl. Phys. Express **13**, 065509 (2020).
- ³⁴ K. Frei, R. Trejo-Hernández, S. Schütt, L. Kirste, M. Prescher, R. Aidam, S. Müller, P. Waltereit, O. Ambacher, and M. Fiederle, Jpn. J. Appl. Phys. **58**, SC1045 (2019).

- ³⁵ J.R. Riley, R.A. Bernal, Q. Li, H.D. Espinosa, G.T. Wang, and L.J. Lauhon, ACS Nano **6**, 3898 (2012).
- ³⁶ D.R. Diercks, B.P. Gorman, R. Kirchhofer, N. Sanford, K. Bertness, and M. Brubaker, J. Appl. Phys. **114**, 184903 (2013).
- ³⁷ E.D. Russo, I. Blum, J. Houard, M. Gilbert, G. Da Costa, D. Blavette, and L. Rigutti, Ultramicroscopy **187**, 126 (2018).
- ³⁸ D.J. Larson, T.J. Prosa, R.M. Ulfig, B.P. Geiser, and T.F. Kelly, *Local Electrode Atom Probe Tomography* (Springer New York, New York, NY, 2013).
- ³⁹ F. Tang, M.P. Moody, T.L. Martin, P.A.J. Bagot, M.J. Kappers, and R.A. Oliver, Microscopy and Microanalysis **21**, 544 (2015).
- ⁴⁰ S.M. Knoll, S.K. Rhode, S. Zhang, T.B. Joyce, and M.A. Moram, Appl. Phys. Lett. **104**, 101906 (2014).